ELSEVIER

Sensors and Actuators B 79 (2001) 107–114

SENSORS AND ACTUATORS B CHEMICAL

www.elsevier.com/locate/sensorb

Fabrication and characterization of electroosmotic micropumps

Shulin Zeng[a,*], Chuan-Hua Chen[b], James C. Mikkelsen Jr.[b], Juan G. Santiago[b]

[a]*Aclara Biosciences, 1288 Pear Avenue, Mountain View, CA 94043, USA*
[b]*Department of Mechanical Engineering, Stanford University, Stanford, CA 94305, USA*

Received 18 January 2001; received in revised form 5 May 2001; accepted 10 May 2001

Abstract

Electroosmotic flow (EOF) micropumps which use electroosmosis to transport liquids have been fabricated and used to achieve pressures in excess of 20 atm and flow rates of 3.6 μl/min for 2 kV applied potentials. These pumps use deionized water as working fluids in order to reduce the ion current of the pump during operation and increase thermodynamic efficiency. EOF pumps are fabricated by packing the 3.5 μm diameter non-porous silica particles into 500–700 μm diameter fused-silica capillaries and by using a silicate frit fabrication process to hold the particles in place. The devices have no moving parts and can operate as both open (high flow rate) and closed (high pressure) systems. Pressure versus flow rate performance data are presented and combined with measurements of physical dimensions, dry and wet weight, and ion current to calculate the pump structure porosity, tortuosity, effective pore radius, and zeta potential.

Keywords: Electrokinetic; Electroosmotic; Micropump; High pressure

1. Introduction

The application of micro-electro-mechanical systems (MEMS) technology to microfluidic devices, such as microelectronic cooling systems and bioanalytical systems, has spurred the development of micropumps to transport a variety of liquids at a large range of flow rates and pressures. A number of micropumps have been designed and built using emerging microfabrication technologies [1,2]. Many of these can be classified into two groups: membrane-displacement pumps and field-induced flow pumps. In membrane displacement pumps, the deflection of microfabricated membranes (e.g. silicon diaphragms) provides the pressure work for the pumping of liquids. Membrane pumps may be further classified based on how the membranes are actuated, including piezoelectric [3–8], electrostatic [9–11], thermopneumatic [12], electromagnetic [13], and photothermally actuated pumps [14]. Membrane micropumps are also differentiated by the variety of valving schemes often used to rectify the flow through the pump, such as dynamic passive valves [15] and other types [1]. Field-induced flow pumps include electroosmotic [16,17], electrohydrodynamic [18–20], and magnetohydrodynamic [21,22] pumps. Ultrasonic flexural plate waves [23,24] and the liquid displacement of bubbles [25,26] have also been used to propel liquids in microchannels. A clear advantage of field-induced pumps over membrane pumps is that they do not require moving parts, such as check valves, which complicate the fabrication, sealing, and operation of these systems.

Although all the pumps described above can deliver liquids at a wide range of flow rates, only electroosmotic flow (EOF) pumps [16,17] can typically generate pressure differences significantly greater than 1 atm. One exception to this pressure-limitation is a recently described piezoelectric pump [8] reported to generate a maximum differential pressure of 3 atm (and a maximum, no load, flow rate of 3 ml/min) at a peak-to-peak voltage of 1200 V ac at 3.5 kHz.

Paul et al. [16] reported packed capillary EOF pumps whose basic structure is very similar to packed columns used in capillary electrochromatography. For example, one of their pumps, fabricated from a fused-silica capillary of unspecified inner diameter, was packed with 1.5 μm silica particles and generated about 0.035 μl/min flow rate and 10 atm pressure at 1.5 kV applied voltage. A second type of EOF pump, called a parallel plate pump, has been demonstrated which does not use porous structures [17]. The parallel plate pump device uses a wide, shallow channel etched in glass to generate maximum pressures and flow rates of 1.5 atm and 2.5 ml/min at 3 kV, respectively. This planar EOF pump has the advantage of a simple design that can be integrated with other planar microfluidic components.

* Corresponding author.
E-mail address: szeng@aclara.com (S. Zeng).

0925-4005/01/$ – see front matter
PII: S0925-4005(01)00855-3

This paper presents a detailed description of the fabrication of relatively large diameter (>500 μm inner diameter) EOF pumps and describes the low- and high backpressure operation of the pump. We show how the physical properties of the pump, which include tortuosity, porosity, effective pore diameter, and zeta potential of the pumping surfaces, can be derived from the flow-pressure data in combination with measurements of resistivity and wet versus dry weight. We also discuss strategies for the optimization of EOF pump performance based on physical geometry and the properties of the working fluid.

2. Theory

Most surfaces spontaneously develop an electric double layer (EDL) when brought into contact with either weak and strong electrolyte solutions [27]. This charge generation is caused by electrochemical reactions at the liquid/solid interface, and in the case of glass surfaces, the main reaction is the deprotonation of acidic silanol groups which produces a negatively charged wall as shown schematically in Fig. 1. Counter ions from the bulk liquid are attracted to and shield these wall charges. Dissolved co-ions are likewise repelled from the wall. The high capacitance charged region of ions at the liquid/solid interface is called the EDL. The ions in the inner layer of counter ions adjacent to the wall are immobile and called the Stern layer. The outer, diffuse part of the layer is called the Gouy–Chapman layer and forms a net positive region of ions that span a distance on the order of the Debye length of the solution. The Debye length, λ, is about 10 nm from the wall for symmetric univalent electrolytes at 1 mM concentration [27]. When an external electric field is applied parallel to the wall, ions will move in response to the field and drag surrounding liquid with them. This ion drag causes a net motion of bulk liquid along the wall that is called electroosmotic flow. The velocity profile caused by electroosmotic flow in a glass channel is shown schematically in Fig. 1 for the case of a double layer that is thinner than the pore through which the liquid is flowing. The fluid velocity of the region of net charge associated with the EDL increases rapidly from the no-slip condition at the wall to a maximum value near the center of the pore. The EOF micropumps

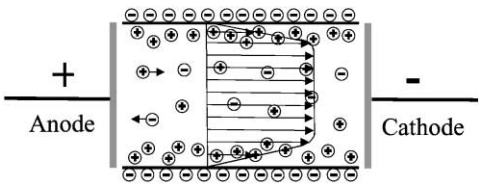

Fig. 1. Schematic illustration of electroosmotic flow through a pore with a finite EDL. The negative charges on the wall depict the deprotonated silanol groups which are shielded by positive counter ions. The positive and negative charges near the center of the pore depict the regions of (net) electrically neutral solution which contributes to Joule heating.

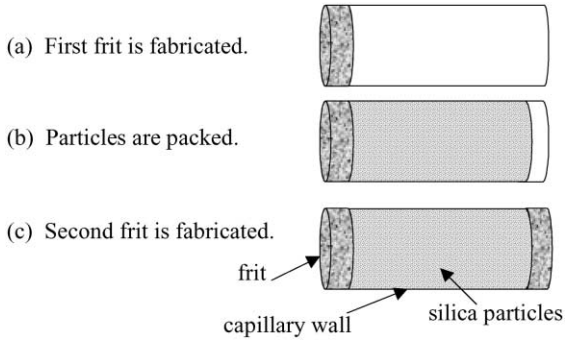

Fig. 2. Packing procedures for fabricating capillary EOF pumps: (a) the first frit is fabricated using a sodium silicate paste and heated in an oven 350°C for 20 min; (b) a particle slurry is pumped into the capillary and the frit retains the 3.5 μm diameter non-porous silica particles; (c) the second frit is fabricated by heating the end of the packed-particle column with a thermal wire stripper.

described here are fabricated using capillaries packed with silica particles and held in place with filter-like "frits" at each end, as shown in Fig. 2. In this porous glass structure, the interstitial spaces between the particles in the packed column act like multiple flow passages in parallel. The high surface-to-volume ratio associated with this porous structure allows for the generation of high pressures.

In the present work we model the structure of porous media as an array of N capillaries with inner radius equal to the average pore radius of the medium, a, and with the length of the tortuous flow path through the pores, L_e [28,29]. To each of these idealized capillaries, we will apply the analytical solution for electroosmotic flow in a single tube with finite EDLs to estimate the behavior of electroosmotic flow in a porous medium. The electroosmotic profile of a liquid in a single capillary under a potential gradient, $E = V/L_e$, and a pressure gradient, $P_z = \Delta P/L_e$, is given by Rice and Whitehead for a capillary of radius, a as [30]

$$v_z(r) = \frac{P_z}{4\mu}(a^2 - r^2) - \frac{\varepsilon\varsigma E}{\mu}\left(1 - \frac{\phi(r/\lambda)}{\zeta}\right) \quad (1)$$

where ε and μ are the dielectric constant and viscosity of the liquid, ς the zeta potential of the particles (which make up the "walls" of the interstitial channels), P_z the uniform pressure gradient along the flow direction z, E the uniform electrical field, and ϕ the potential in the capillary. The non-dimensional potential distribution associated with electric double layer ions, ϕ/ζ, can be calculated by numerically solving the Poisson–Boltzmann equation for a cylindrical geometry [27]. In order to simplify the analysis presented here and derive a closed-form solution of the volume flow rate associated with each pore, we will make the Debye–Huckle approximation that the potential energy associated with each double layer ion is small compared with the kinetic energy of the ions such that the ratio $ze\phi/kT \ll 1$. As pointed out by Hunter [27], this approximation holds surprisingly well even for values of $ze\phi/kT$ equal to about 2, or $\zeta = 50$ mV potentials for monovalent ions at room

temperature. For Debye–Huckle charge layers, the non-dimensional potential is given by Rice and Whitehead as

$$\phi(r/\lambda) = \zeta \frac{I_0(r/\lambda)}{I_0(a/\lambda)}$$

where I_0 is the zero-order modified Bessel function of the first kind. Integrating Eq. (1) for $v_z(r)$ over a cross-section gives the volume flow rate in a single capillary

$$q = 2\pi \int_0^a v_z(r) r \, dr = \frac{\pi P_z a^4}{8\mu} - \frac{\pi \varepsilon \zeta E a^2}{\mu} \left(1 - \frac{2\lambda I_1(a/\lambda)}{a I_0(a/\lambda)}\right) \tag{2}$$

where I_1 is the first-order modified Bessel function of the first kind. The flow rate of the porous medium, Q, which is calculated for N of these capillaries as

$$Q = Nq = N\left[\frac{\pi P_z a^4}{8\mu} - \frac{\pi \varepsilon \zeta E a^2}{\mu} \left(1 - \frac{2\lambda I_1(a/\lambda)}{a I_0(a/\lambda)}\right)\right] \tag{3}$$

Two parameters can be defined to convert the dimensions of the actual tortuous-path pore channels to the physical dimensions of the porous medium. First, tortuosity is defined as $\tau = (L_e/L)^2$, where L_e is the average length of travel for flow along the pore path and L the physical length of the porous structure. The second parameter is porosity, defined as $\psi = U_e/U$, where U_e and U are the void and total volumes of the porous medium, respectively. The effective cross-sectional area of the porous medium is then simply approximated as $A_e = \psi A/\sqrt{\tau}$, where A is the cross-sectional area of the porous medium [29,31]. The flow rate of the entire porous medium is then

$$Q = -\frac{\psi \Delta P A a^2}{8\mu L \tau} - \frac{\psi \varepsilon \zeta V A}{\mu L \tau} \left(1 - \frac{2\lambda I_1(a/\lambda)}{a I_0(a/\lambda)}\right) \tag{4}$$

where ΔP is the pressure difference (downstream minus upstream) along the length of the capillary. The maximum pressure ΔP_m generated across the porous structure is obtained from Eq. (2) or (4) for the condition of zero net flow rate ($Q = 0$)

$$\Delta P_m = \frac{8\varepsilon \zeta V}{a^2} \left(1 - \frac{2\lambda I_1(a/\lambda)}{a I_0(a/\lambda)}\right) \tag{5}$$

The maximum flow rate Q_m of the entire porous medium under the condition of zero counter pressure is

$$Q_m = \frac{\psi \varsigma}{\tau} \frac{\varepsilon V A}{\mu l} \left(1 - \frac{2\lambda I_1(a/\lambda)}{a I_0(a/\lambda)}\right) \tag{6}$$

Substituting Eqs. (5) and (6) into (4), a linear relationship between the flow rate and the pressure of an EOF pump is obtained

$$Q = Q_m \left(\frac{\Delta P}{\Delta P_m} - 1\right) \tag{7}$$

This linear relationship is a result of the linear superposability of the flow rates associated with electroosmosis and pressure driven flow.

For a given applied voltage, and a choice of particle material and working fluid (which fixes ε, ζ, and μ), Eq. (5) indicates that the pressure is inversely proportional to the square of the pore radius. For the packings we have investigated, pore size is proportional to the particle radius. Similarly Eq. (6) indicates that higher flow rates result from large cross-sectional area and short pump lengths.

The porosity can be determined experimentally from the wet and dry weights of the pump, wt_{wet} and wt_{dry}, using

$$\psi = \frac{wt_{wet} - wt_{dry}}{\rho A L} \tag{8}$$

where ρ is the density of water.

Eqs. (5) and (6) can be rearranged to give the ratio

$$\kappa = \frac{Q_m}{\Delta P_m} = \frac{A}{8\mu l} \frac{\psi a^2}{\tau} \tag{9}$$

which can be determined experimentally from the slope of a plot of Q versus ΔP for a given pump. Eq. (9) therefore contains known physical parameters of A, μ, and L; an experimentally determined κ; and the unknowns ψ, a, and τ.

A third expression involving ψ and τ can be derived from the ratio of the electrical resistance of an empty (unpacked) capillary to that of a packed capillary; each containing liquid with the same resistivity. Our approach is similar to that suggested by Rathore et al. [31]. The resistances of empty (R_{em}) and packed (R_{pack}) capillaries are $\omega L/A$ and $\omega L_e/A_e$, respectively, where ω is the resistivity. The ratio of R_{em}/R_{pack} is then LA_e/L_eA, which reduces to

$$\frac{R_{em}}{R_{pack}} = \frac{\psi}{\tau} \tag{10}$$

by the definition of the tortuosity and the porosity. Once ψ is measured using Eq. (8), τ can be determined from the experimental resistance ratio and Eq. (10). The pore size, a can be determined from the experimental value of κ and Eq. (9). ζ can be determined from either Eq. (5) or (6).

Lastly, an important characteristic of the pump is its thermodynamic efficiency, η, which we define as simply

$$\eta = \frac{\Delta P Q}{VI} \tag{11}$$

The efficiency is the ratio of the useful pressure work, ΔPQ, to the applied electrical work, VI. The total current I is the sum of Joule current in the bulk liquid and the current associated with electromigration in the EDL. For systems with low Debye length-to-pore diameter ratios (i.e. thin double layers), the total current is approximately equal to the Joule current in the bulk so that $I \cong \sigma_{bulk} A_e E$. Applying Eq. (3) and the thin-double-layer approximation, the efficiency becomes

$$\eta \cong \frac{\varepsilon \zeta \Delta P}{\mu \sigma V}$$

This simple model suggests that thermodynamic efficiency is inversely proportional to the product of viscosity

and bulk conductivity. However, since the latter is also inversely proportional to viscosity, there is no net dependence of η on viscosity, and thus η is only weakly dependent on temperature. Note that the generated pressure in the equation is also a function of zeta potential so that the efficiency scales as ζ^2.

For the pumping conditions described in this paper, the area of the double layers is on the order of the bulk flow area outside of the double layer. The total current should, therefore, be calculated from a detailed analysis of the double layer ion distribution. Although this analysis is beyond the scope of this paper, we will present the efficiency of our pump as obtained from direct measurements of ΔP, Q, V, and I.

3. Fabrication

EOF micropumps were fabricated by packing fused-silica capillaries (Polymicro Technologies Inc., Phoenix, AZ) with non-porous silica particles (Bangs Labs Inc., Fishers, IN, and Micra Scientific Inc., Darien, IL), as shown schematically in Fig. 2. The first step is to make a 1 mm long retaining frit (Fig. 2a) at one end of the capillary by packing a cohesive paste made up of one part sodium silicate solution (14% NaOH aqueous solution, Sigma) and three parts non-porous silica particles and baking the capillary in an oven at 350°C for 20 min. As the paste dries, a silicate deposit adheres strongly to both the beads and capillary wall, and the frit is formed. Once the frit is in place, the other end of the capillary is connected to a pressure-driven slurry packing system using plastic or stainless steel fittings (Upchurch Scientific, Oak Harbor, WA, and Alltech Associates Inc., Deerfield, IL), as shown schematically in Fig. 3. A schematic of the pressure-driven, slurry-packing system for EOF micropump fabrication is shown in Fig. 3. An high-pressure liquid chromatography (HPLC) pump (Shimadzu, Pleasanton, CA) drives liquid from a buffer reservoir into a slurry reservoir through stainless steel tubing. In all cases, deionized water was used as a working fluid for the packing of

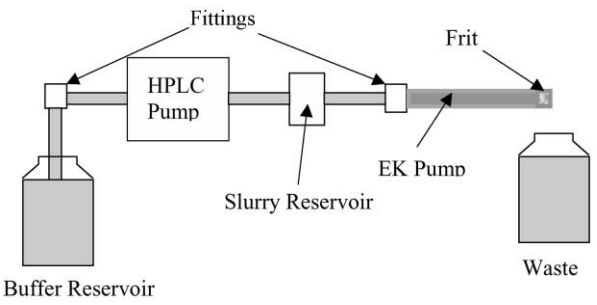

Fig. 3. Setup for fabrication of capillary EOF pumps. A high pressure stream of buffer solution is developed using a HPLC pump. This high pressure buffer stream pumps the slurry into the pump structure. Filtered buffer solution from the slurry is collected in a waste well.

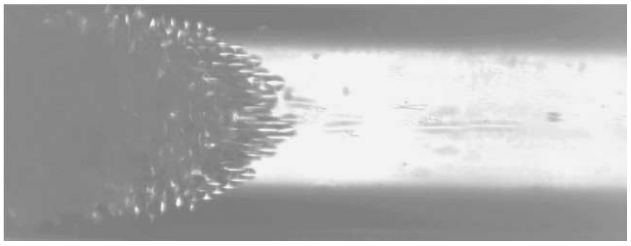

Fig. 4. Particle distribution in a capillary during slurry packing. Flow is from right to left and several particle streaks are visible upstream of the packed column interface. The detrimental effects of the curved particle bed/buffer interface can be reduced by sonification.

columns. The particles and liquid are forced by the flow stream into the capillary, water passes through the frit, and particles are retained in the capillary. After the capillary is packed, pure water is pumped into the system at 50 atm for 30 min to insure the particles are densely packed. After the column is packed with silica particles, (Fig. 2b), a second frit is fabricated in place using a similar procedure (Fig. 2c) except that the second frit is sintered in place using a thermal wire stripper (Digi-Key, Thief River Falls, MN). Heating the second frit locally with a thermal wire stripper instead of an oven prevents sudden and massive evaporation of water retained inside the packed columns. An EOF micropump with two frits and packed particles is shown schematically in Fig. 2c. We have fabricated EOF pumps with inner diameters of 530 and 700 μm. The 700 μm diameter pump columns have twice the diameter of the largest commercially available electrokinetic chromatography columns with similar, packed-bead structures [32].

Fig. 4 shows how 10–20 μm diameter particles (chosen for the purpose of this visualization) are distributed in a 400 μm inner diameter capillary during pressure-driven slurry packing. Particles advected by the parabolic flow upstream of the packed column accumulate near the center of the capillary. We have observed that increasing pressure alone does not change the packing distribution appreciatively. Instead, agitation using an ultrasonic bath was found to be an effective way to achieve a homogeneously packed structure. This method is also effective for smaller particles such as the 3.5 μm diameter particles used in this study as evidenced by the low porosity value obtained below.

4. Results and discussion

Fig. 5 shows the setup used for characterizing the EOF micropumps. A backpressure regulator (Upchurch Scientific, Oak Harbor, WA) and a pressure transducer (Digi-Key, Thief River Falls, MN) were installed at the downstream end of the pump to control flow rate and measure pressure. A 0–30 kV power supply (Unimicro Technologies Inc., Pleasanton, CA) is connected to Pt wire electrodes. The EOF pumps are typically filled (i.e. primed) by an HPLC pump or by a manual pump (Unimicro Technologies Inc., Pleasanton,

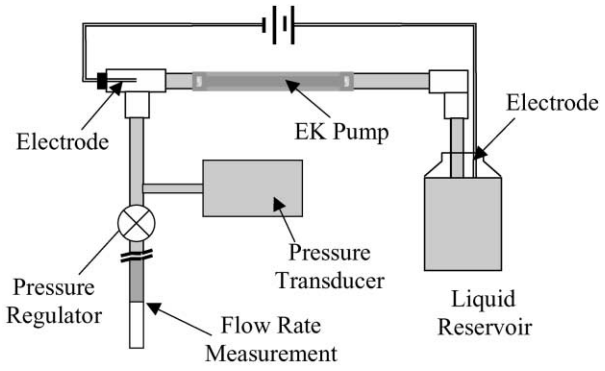

Fig. 5. Schematic of setup for EOF micropump characterization. The EOF pump is used to pump liquid in a tube with an easily observable meniscus to measure volume flow rate. A pressure regulator is used to impose a range of counter-pressures on the pump which can be measured with a pressure transducer.

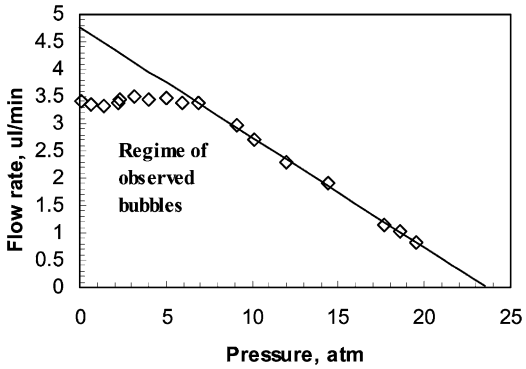

Fig. 6. Flow rate vs. measured backpressure (symbols) in experiments and best-fit with measured data at backpressures greater than 7 atm (line). The regime of observed bubbles correlates with a significant drop in the flow rate capacity of the pump. The working fluid is deionized water.

CA). Deionized water, untreated HPLC-grade acetonitrile, and borate buffers have been used as working fluids. The deionized water experiments are described here. Flow rate is measured by tracing the working fluid/air meniscus within a capillary tube of known diameter.

Again, for the experiments described here, the working fluid was deionized water. The measured pH and conductivity of the deionized water are 5.7 and 3.0 μS/cm, respectively. Storage and handling of deionized water often result in a slight decrease of pH to approximately 5.7 [33] and an increase in conductivity. This is due to absorption of atmospheric carbon dioxide and the subsequent generation and solution of carbonic acid. We can estimate the ionic concentration of our deionized water based on this conductivity by assuming a mobility for the impurity ions. For example, for impurity ions with mobilities equal to that of potassium chloride and carbonic acid, the estimates of ion densities are 10 and 7.5 μM, respectively. For the calculations presented here, we will assume that the impurity ions are similar to carbonic acid and use the 7.5 μM estimate. Note that we could easily add buffer ions to our working fluid in order to make the estimate of ionic conductivity more accurate, but we chose not to do this in order to minimize Joule heating of the working fluid and maximize thermodynamic efficiency of the pump. The Debye length of this solution is about 0.11 μm, or approximately one-fifth of the effective pore radius determined below.

Fig. 6 shows a plot of the flow rate versus backpressure for 2 kV applied to a pump that is 530 μm in diameter, 5.4 cm long, and packed with 3.5 μm non-porous silica particles. The maximum pressure generated by this pump is 23.5 atm; the solid line is a linear fit for data points with backpressures larger than 7 atm; and the extrapolated maximum flow rate from the linear fit is 4.8 μl/min. The current in the pump circuit is measured to be 1.8 μA. The thermodynamic efficiency, defined by Eq. (11), is 1.3% for $Q = 0.5Q_m$, $\Delta P = 0.5\Delta P_m$, which is the optimal operating condition in terms of thermodynamic efficiency.

As shown in Fig. 6, the pump flow rate is nearly constant at low backpressures. We used transparent fittings and tubes to observe electrolytic hydrogen bubble generation at the cathode when the backpressure was below 7 atm. In this pressure range there was also a noticeable decrease in the electrical current, which suggests that there may also be bubbles in the body of the pump. As shown by Eq. (1), at high backpressure the flow profile shows a reverse flow with negative (upstream) velocities near the centerline of the pores. Therefore, at high backpressure there may be sufficient pressure-driven reverse flow in the pump to recirculate electrolytically-generated gases (dissolved and undissolved), which can react together or at the electrodes to form water.

The slope of the line in Fig. 6 is the ratio of the maximum flow rate to the maximum pressure, defined as κ in Eq. (9), and has an experimental value of 0.20 μl/(min-atm). Using the pump length and area of 5.4 cm and 2.2E−3 cm^2, respectively, and a value of 1.0E−3 Pa s for the viscosity of water at 20°C, Eq. (9) leads to a value of $\psi a^2/\tau = 6.7 \times 10^{-10}$ cm^2. This term will be used below with porosity and resistance ratio to determine the tortuosity, effective pore radius, and zeta potential.

Wet and dry weights of the devices were measured and the porosity was found to be 0.37 using Eq. (8). This value is substantially greater than the 0.26 characteristic of ideal hexagonally-closed-packed or face-centered-cubic packing of spheres and is comparable to other reported values for random packing of nearly monodispersed spheres. For example, Sen et al. [34] reported a porosity of 0.40 for their packed beds.

Fig. 7 shows voltage versus current for an empty and a packed capillary using a saturated KCl solution. At high ionic strength (we used a value of approximately 4 M) the ionic conduction dominates any advected current from EOF. Both capillaries were 700 μm in diameter and 4.6 cm in length. One of the capillaries was empty and the other packed with 3.5 μm non-porous silica particles using the

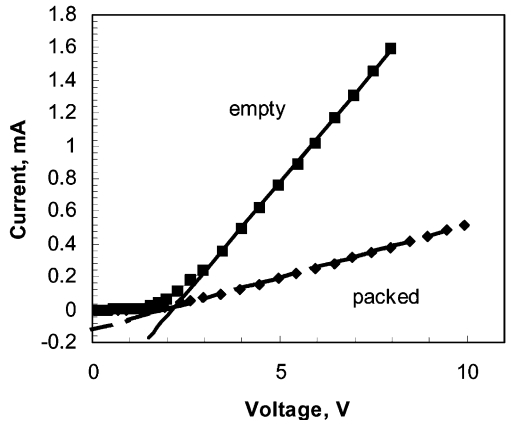

Fig. 7. Electric potential vs. current for an empty capillary section and a packed capillary (both filled with saturated KCl solutions). The slope of the curves after the initial, non-linear low-voltage region are a measurement of the electrical resistance of the devices. The working fluid is saturated KCl solution.

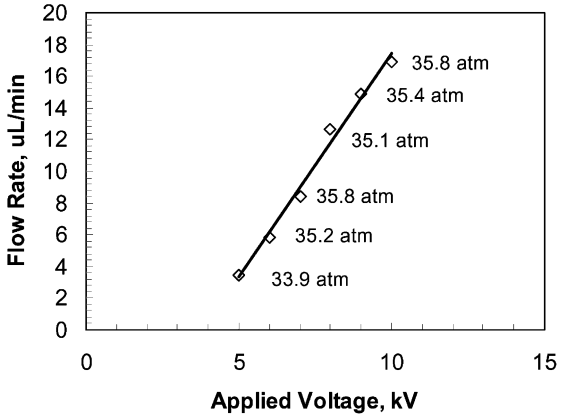

Fig. 8. Flow rates vs. applied voltages for a back pressure fixed at approximately 35 atm. The symbols are from experiments and the line is the best fit of the data. The working fluid is deionized water.

same packing process described above for the 530 μm capillaries. The initial non-linearity of the curves is due to over-potential at the electrodes [35]. We used the linear data after 3 V to calculate the electric resistances: the resistance ratio is 0.24. This value is slightly lower than the 0.29 and 0.28 values obtained by Rathore et al. [31] for pressure-packed capillaries of 2 or 6 μm silica particles, respectively. Using Eq. (10) and the 0.37 porosity measured for this type of packing, we obtain a tortuosity of 1.5, which is within the range reported in literature [29]. Inserting these values into Eq. (9), we obtain 0.53 μm, for the effective pore radius. Finally, applying our measurements to Eq. (3) or (4), we obtain a value of −95 mV for the zeta potential. This value of zeta potential compares fairly well with the value of −90 mV reported by Scales et al. [33] for silica plates in low ionic strength, pH 5.8 solutions.

Table 1 summarizes the parameters determined in this paper and those obtained from the literature. Note that, as a qualitative description of our method, critical experiments for each parameter are listed but the determination of several parameters, such as tortuosity and zeta potential, requires multiple experiments.

We have also studied the flow rate performance of the EOF pump at fixed back pressure. Fig. 8 gives flow rates versus applied electric voltage for a 35 atm back pressure.

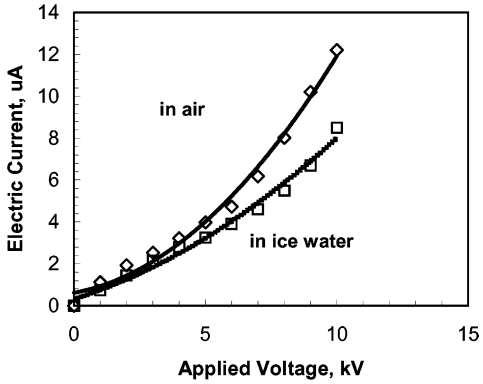

Fig. 9. Electric current vs. applied voltage with the fluid reservoir in the air at room temperature (diamonds) and in ice water at 0°C (squares). The lines are a simple spline fit through the data. The slope of the current vs. voltage profiles are nearly equal at low voltages where Joule heating is negligible. The working fluid is deionized water.

Because of limitations of the pressure regulator, the back-pressure varied slightly and measured pressures are labeled at each data point. At 5 kV, the flow rate is about 3.5 μl/min, and the flow rate reaches 17 μl/min at 10 kV. The linear trend between flow rate and applied electric voltage is predicted by Eq. (4). The slight non-linearity in these measurements is probably caused due to the slight variations in back pressure.

Table 1
List of parameters

Parameter (unit)	Value	Critical experiment or source
Working fluid viscosity, μ (Pa s)	1.0E−3	[28]
Working fluid dielectric constant, ε (C^2/J/m)	6.9E−10	[28]
Conductivity of working fluid, σ (μS/cm)	3.0	Ionic conductivity meter
Zeta potential, ζ (mV)	−95	Q vs. ΔP measurements
Effective pore radius of packed bed, a (μm)	0.53	Q vs. ΔP measurements
Porosity of pump, ψ	0.37	Dry vs. wet weight of porous structure
Tortuosity of pump, τ	1.5	High salt solution current measurement
Thermodynamic efficiency, η	1.3%	Measurement of each quantity in Eq. (11)

Fig. 9 shows electric currents versus applied electric voltages. In one of the experiments shown here, the working fluid reservoir is exposed to air at standard conditions. In a second experiment, the reservoir is submerged in ice water at 0°C. As expected, the currents are higher for the higher working fluid temperature because ionic conductivity is inversely proportional to viscosity, which decreases about 2% for each 1°C rise in temperature. Cooling of EOF pumps may be a viable method for preventing boiling at high field conditions and extending the performance characteristics of the pump.

5. Conclusions and future work

EOF pumps were fabricated by packing the 3.5 μm diameter non-porous silica particles into 500–700 μm diameter fused-silica capillaries and using a silicate frit fabrication scheme to hold the particles in place. These pumps have no moving parts and can generate maximum pressures in excess of 20 atm or maximum flow rates of 3.6 μl/min for a 2 kV applied potential. Thermodynamic efficiency is approximately inversely dependent on the conductivity of the working fluid, and so we have characterized our pumps with deionized water as the working fluid. We achieve a thermodynamic efficiency of 1.3%. The porosity of the packing was determined from the dry and wet weights of the pump to be 0.37, and is in agreement with expectations for random packing of spherical particles. The measured ratio of resistivities for packed and unpacked capillaries was 0.24, in agreement with similar measurements in the literature. From a simple expression for the resistivity ratio in terms of porosity and tortuosity, we derive a value of 1.5 for the tortuosity. From the experimental slope of the pressure-flow rate curves and the above parameters we are able to derive the effective pore radius for our pumps to be 0.53 μm. From our measurements of ΔP or Q, we determined that the zeta potential for our packed capillaries was −95 mV.

The simple flow model presented here suggests how to optimize the design of an EOF pump to deliver a range of flowrates and pressures. For a given voltage, working fluid, and particle composition, the pressure is dependent primarily on the inverse square of the particle radius. By replacing the 3.5 μm diameter particles of our pumps with 1 μm particles, we can expect a factor of 10 increase in pressure. Since Q is independent of particle (pore) size, the flow rate should not decrease as the pore structure gets finer, so long as the packing structure parameters of porosity and tortuosity also remain unchanged. Similarly, a higher flow rate will result from an increase in the cross-section area of the pump and/or a decrease in the length, without too much of an effect on the generated pump pressure. We are currently developing pumps which are greater than 1 cm in diameter and only a few millimeter long in order to achieve our ultimate goals of flow rates in the range of 1–10 ml/min and 10 atm pressure capacity. We are also investigating other aspects of EOF micropumps, which include eliminating the limitations associated with electrolytic gases and improving the long-term performance of the devices.

Acknowledgements

This work was supported by DARPA under Contract no. F33615-99-C-1442 with Dr. Elias Towe as contract monitor. The authors thank Mac Schwager for assistance in making pump frits, Dr. Chao Yan of Unimicro Technologies Inc. for valuable discussions about fabrication and operation of EOF pumps, and Ms. Jing-Ran Chen for help in building the packing system.

References

[1] S. Shoji, M. Esashi, Microflow devices and systems, J. Micromech. Microeng. 4 (1994) 157.
[2] P. Gravesen, J. Branebjerg, O.S. Jensen, Microfluidics — a review, J. Micromech. Microeng. 3 (1993) 168.
[3] H.T.G. van Lintel, F.C.M. van de Pol, S. Bouwstra, A piezoelectric micropump based on micromaching of silicon, Sens. Actuators A 15 (1988) 153.
[4] V. Gass, B.H. Vanderschoot, S. Jeanneret, N.F. Derooij, Integrated flow-regulated silicon micropump, Sens. Actuators A 43 (1994) 335.
[5] M.C. Carroza, N. Croce, B. Magnani, P. Dario, A piezoelectric-driven stereolithography-fabricated micropump, J. Micromech. Microeng. 5 (1995) 177.
[6] M. Koch, N. Harris, A.G.R. Evans, N.M. White, A. Brunnschweiler, A novel micromachined pump based on thick-film piezoelectric actuation, Sens. Actuators A 70 (1998) 98.
[7] M. Richter, M. Linnemann, P. Woias, Robust design of gas and liquid micropumps, Sens. Actuators A 68 (1998) 480.
[8] H.Q. Li, D.C. Roberts, J.L. Steyn, K.T. Turner, J.A. Carretero, O. Yaglioglu, Y.H. Su, L. Saggere, N.M. Hagood, S.M. Spearing, M.A. Schmidt, R. Mlcak, K.S. Breuer, A high frequency high flow rate piezoelectrically driven MEMS micropump, in: Proceedings of the Solid-State Sensor and Actuator Workshop, Hilton Head Island, SC, 4–8 June 2000.
[9] T. Bourouina, A. Bosseboeuf, J.P. Grandchamp, Design and simulation of an electrostatic micropump for drug-delivery applications, J. Micromech. Microeng. 7 (1997) 186.
[10] O. Francais, I. Dufour, E. Sarraute, Analytical static modeling and optimization of electrostatic micropumps, J. Micromech. Microeng. 7 (1997) 183.
[11] N.T. Nguyen, S. Schubert, S. Richter, W. Dotzel, Hybrid-assembled micro dosing system using silicon-based micropump/valve and mass flow sensor, Sens. Actuators A 69 (1998) 85.
[12] O.C. Jeong, S.S. Yang, Fabrication and test of a thermopneumatic micropump with a corrugated p plus diaphragm, Sens. Actuators A 83 (2000) 249.
[13] Q.L. Gong, Z.Y. Zhou, Y.H. Yang, X.H. Wang, Design, optimization and simulation on microelectromagnetic pump, Sens. Actuators A 83 (2000) 200.
[14] H. Mizoguchi, M. Ando, T. Mizuno, T. Takagi, N. Nakajima, Design and fabrication of light driven micropump, in: Proceedings of the IEEE-MEMS Workshop, 1992, pp. 31–36.
[15] T. Gerlach, Microdiffusers as dynamic passive valves for micropump applications, Sens. Actuators A 69 (1998) 181.
[16] P.H. Paul, D.W. Arnold, D.J. Rakestraw, Electrokinetic generation of high pressures using porous microstructures, μ-TAS 98, Banff, Canada, 1998.

[17] C.-H. Chen, S. Zeng, J.C. Mikkelsen, J.G. Santiago, Development of a planar electrokinetic micropump, in: Proceedings of the ASME International Mechanical Engineering Congress and Exposition, Orlando, USA, 2000.
[18] A. Richter, H. Sandmaier, Electrohydrodynamic Pumping and Flow Measurement, in: Proceedings of the IEEE-MEMS Workshop, 1991, pp. 99–104.
[19] S.F. Bart, L.S. Tavrow, M. Mehregany, J.H. Lang, Microfabricated electrohydrodynamic pumps, Sens. Actuators A A21–A23 (1990) 193.
[20] G. Fuhr, R. Hagedorn, T. Muller, W. Benecke, B. Wagner, Travelling wave-driven microfabricated electrohydrodynamic pumps for liquid, J. Micromech. Microeng. 4 (1992) 217.
[21] L. Huang, W. Wang, M.C. Murphy, K. Lian, Z. Ling, Design, microfabrication and test of a magnetohydrodynamic micropump, in: Proceedings of the SPIE 1999 Symposium and Education Program on Micromaching and Microfabrication, Santa Clara, CA, 1999.
[22] A.V. Lemoff, A.P. LeeP, An ac magnetohydrodynamic micropump, Sens. Actuators B 63 (2000) 178.
[23] N.T. Nguyen, R.M. White, Design and optimization of an ultrasonic flexural plate wave micropump using numerical simulation, Sens. Actuators A 77 (1999) 229.
[24] N.T. Nguyen, A.H. Meng, J. Black, R.M. White, Integrated flow sensor for in situ measurement and control of acoustic streaming in flexural plate wave micropumps, Sens. Actuators A 79 (2000) 115.
[25] T.K. Jun, C.J. Kim, Valveless pumping using traversing bubbles in microchannels, J. Appl. Phys. 83 (1998) 5658.
[26] H. Yuan, A. Prosperetti, The pumping effect of growing and collapsing bubbles in a tube, J. Micromech. Microeng. 9 (1999) 402.
[27] R.J. Hunter, Zeta Potential in Colloid Science, Principles and Applications, Academic Press, New York, 1981.
[28] R.F. Probstein, Physicochemical Hydrodynamics, Wiley, New York, 1994.
[29] J. Bear, Dynamics of Fluids in Porous Medium, Dover, New York, 1972.
[30] C.L. Rice, R. Whitehead, Electrokinetic flow in a narrow cylindrical capillary, J. Phys. Chem. 69 (1965) 4017.
[31] A.S. Rathore, E. Wen, C. Horvath, Anal. Chem. 71 (1999) 2633.
[32] Product Catalog, Unimicro Technologies Inc., Pleasanton, CA.
[33] P.J. Scales, F. Grieser, T.W. Healy, L.R. White, D.Y.C. Chan, Electrokinetics of the silica solution interface: a flat-plate streaming potential study, Langmuir 8 (1992) 965.
[34] P.N. Sen, C. Sclaa, M.H. Cohen, A self-similar model for sedimentary-rocks with application to the dielectric-constant of fused glass-beads, Geophysics 46 (1981) 781.
[35] D.W. Oxtoby, N.H. Nachtrieb, Principles of Modern Chemistry, Saunders, London, 1990.